Indian Journal of Pure & Applied Physics
Vol. 52, October 2014, pp. 689-698

Calorimetric and dielectric study of a negative dielectric anisotropy alkoxy-phenyl-benzoate liquid crystal

P Kalakonda[1,2], H Kashuri[1], K Kashuri[1] & G S Iannacchione[1]*

[1]Department of Physics, Worcester Polytechnic Institute, Worcester, MA 01609, USA

[2]Department of Material Science and Engineering, Carnegie Mellon University, Pittsburgh, PA 15213, USA

*E-mail: parvathalu.k@gmail.com

Received 7 May 2014; revised 6 August 2014; accepted 2 September 2014

Modulated Differential Scanning Calorimetry (MDSC) and dielectric spectroscopy have been used to measure the complex specific heat and dielectric constant over a wide temperature range on heating and cooling for a negative dielectric anisotropy alkoxyphenylbenzoate liquid crystal, denoted 9OO4. The MDSC experimental parameters were varied in order to yield quasi-static specific heat results and the same base scan rate was used for the dielectric measurements. On cooling, 9OO4 exhibits a typical weakly first-order isotropic to nematic then a continuous nematic to smectic-*A* phase sequence followed by a monotropic smectic-*C* and smectic-*B* phases before crystallizing. The smectic-*B* conversion is very slow, even for our quasi-static scan parameters. On heating, the crystal phase super-heats and exhibits a strong first-order transition into an unknown smectic phase that itself converts to the smectic-*A* phase via a first-order, highly rate dependent, phase transition. The nematic-smectic-*A* transition has an unusual character given the molecular structure of 9OO4 that may be related to combination of molecular structure and a negative dielectric anisotropy.

Keywords: Calorimetry, Dielectric spectroscopy, Phase behaviour, Liquid crystal

I Introduction

The study of liquid crystals affords a unique opportunity to connect microscopic character of the molecule to the macroscopic phase ordering of the ensemble[1-4]. The single feature of molecular anisotropy leads to two thermodynamically stable phases between the isotropic and a full three-dimensionally ordered solid phases. These two are the nematic (*N*) phase that exhibits only orientational order due to alignment of LC molecules and the smectic-*A* (Sm*A*) phase where the molecules are arranged in liquid-like layers and so exhibit partial translational order characterized by 1-d density wave. However, liquid crystal ordering is much richer (chirality, layer spacing versus molecule length, molecule tilt with respect to the layer normal, in-plane ordering, etc.) and it is of great interest to understand the connection between a microscopic characteristic of the molecule and the resulting macroscopic phase. In addition, the higher order, lower symmetry, mesophases that emerge are not only interesting in their own right, they also provide a rich range of physical model system to explore open questions of self-assembly, interactions with external fields and surfaces as well as multi-component colloidal mixtures[3].

Because the focus is on the connection between the molecule and the phase ordering of the ensemble, there are two general experimental approaches. The first approach is to determine in great detail the molecular structure and dynamics via spectroscopy and the others are the various thermo-physical property measurements of the resulting ordered phases. Typically, the latter types of experiments are more straight-forward while the former requires careful attention to sample preparation and purity. Since most liquid crystals are relatively simple, low molecular weight, organic molecules, molecular modeling using well-established force-fields are easily accessible and can be used to augment thermo-physical experiments and provide guidance to microscopic experiments. Of the various thermo-physical experiments possible in studying phases and phase transitions, calorimetry and dielectric measurements are particularly useful. Here, two experimental techniques were employed, modulated differential scanning calorimetry (MDSC) and dielectric spectroscopy. For MDSC, the sample specific heat is decomposed into reversing (real) and non-reversing (imaginary) components and allows for a consistent definition of dynamic thermal analysis in analogy to dynamic mechanical or dielectric

spectroscopies[5-10] where the complex dynamics is related to either entropy (constant volume) or enthalpy (constant pressure) fluctuations[9]. This complex calorimetric technique details closely with dielectric spectroscopy, which probes at a given frequency the dielectric constant of various modes and so provides a bridge between microscopic and macroscopic measurements.

In the present work, the phase behaviour by calorimetry and dielectric spectroscopy of a negative dielectric anisotropy alkoxyphenylbenzoate liquid crystal denoted by 9OO4, has been studied. This liquid crystal has molecular structure closely similar to two other liquid crystal homologous series pentylphenylthiol alkoxybenzoate (n⁻S5) and alkoxybenzylidene alkylaniline (nO.m). However, 9OO4 has a different linking group between the two aromatic rings and alkoxy groups on both ends, comparatively. The experiments on 9OO4 here reveal some unique features as compared to two well-studied members of these related series, 8S5 and 4O.8. One striking difference as given in the similar structure is that 9OO4 exhibits two monotropic smectic phases, a tilted smectic-*C* (Sm*C*) and an in-plane hexatic ordered smectic-*B* (Sm*B*) between its Sm*A* and crystal phases while 8S5 only has a monotropic Sm*C* phase and 4O.8 has a plastic crystal-*B* (Cr*B*) phase between their monomeric $Sm\mathit{A}_m$ and crystal. The conversion into the Sm*B* phase is very slow, exhibiting strong variations and multiple steps even for very slow scan rates. Also, the *N*-Sm*A* transition in 9OO4 has an unusually small enthalpy of 0.3 J/g as compared to that in 8S5 and 4O.8 of about 2 J/g. The dielectric constant of the Sm*A* phase has a hysteresis begin larger on cooling than heating under identical conditions and so depends on whether the Sm*A* formed from the *N* or crystal phase. Intriguingly, on heating 9OO4 exhibits a stable specific heat and dielectric feature that indicates an intermediate smectic-like phase between the crystal and smectic-*A* phase. The primary difference between 8S5 and 4O.8 with 9OO4 is that the effective dipole moment of all three, though perpendicular to the long molecular axis, is oriented essentially parallel to the plane of the two-phenyl rings of 8S5 and 4O.8 while in 9OO4 it is oriented nearly perpendicular. Not only does the different linking groups in these types of LCs have different structure and flexibility but changes the orientation of the effective dipole moment. This feature may explain the unusual phase ordering.

2 Methodology

The liquid crystal 9OO4 is a phenyl benzoate containing an oxo ester linking group with two alkoxy end groups (Fig. 1). The molecular mass for 9OO4 is M = 424.657 g/mol with an extended molecular structure approximately 4 nm long and 0.8 nm wide. This LC has a structure and molecular weight similar to the relatively well-studied liquid crystals pentylphenylthiol alkoxybenzoate (8S5) and butoxybenzylidene octylaniline (4O.8). For 8S5, the phase sequence (in degrees celsius) is *K*-57.9-Sm*C*-56.1-Sm*A*-63.6-*N*-86.2-*I* while 4O.8 has the phase sequence of *K*-38.4-Cr*B*-49.2-Sm*A*-63.8-*N*-79-*I* where Cr*B* is a plastic crystal-*B* phase and the Sm*C* phase for 8S5 is monotropic to the crystal phase (K). These types of liquid crystal molecules tend to have a negative dielectric anisotropy, the dielectric constant perpendicular to the long molecular axis $\varepsilon_\perp$ is larger than the parallel component $\varepsilon_\parallel$. The anisotropy emerges from the linking group of the two phenyl rings and the presence of alkyl (or alkoxy) end groups[11]. However, the effective dipole moment for 8S5 and 4O.8, though perpendicular to molecular long axis, lies nearly in the plane of the phenyl rings. For 9OO4, the carbon-oxygen double bond in the oxo ester linking group, its effective dipole moment is pointing nearly perpendicular to the plane of the phenyl rings. Note that the rough estimated dipole moment magnitude is the smallest for 8S5 while approximately the same for 4O.8 and 9OO4.

The LC 9OO4 was used as after desired amount of LC was first dispersed in ultra-pure acetone and shaken on a mixer for <30 min followed by sonication for 3 h. Finally, the acetone was evaporated slowly then degassed under a modest vacuum in the isotropic phase of 9OO4 (<364 K or 90°C) for about 2 h before sealing into the experimental cells (Fig. 2). Acetone was chosen as the dispersing solvent because it is compatible with the LC and used in its purification (re-crystallization). This procedure was followed for this pure LC study because this procedure must also

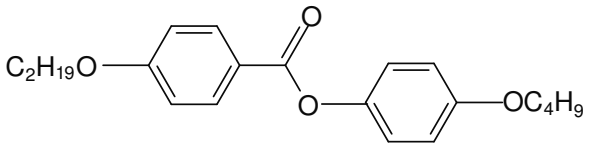

Fig. 1 — Member of the 4-n-alkoxy phenyl-4°-m-alkoxy benzoate homolog series denoted nOOm. In this study, n = 9 and m = 4 (9OO4). Note that the negative dielectric anisotropy is due to the O-C=O group in the benzoate group linking the two phenyl rings

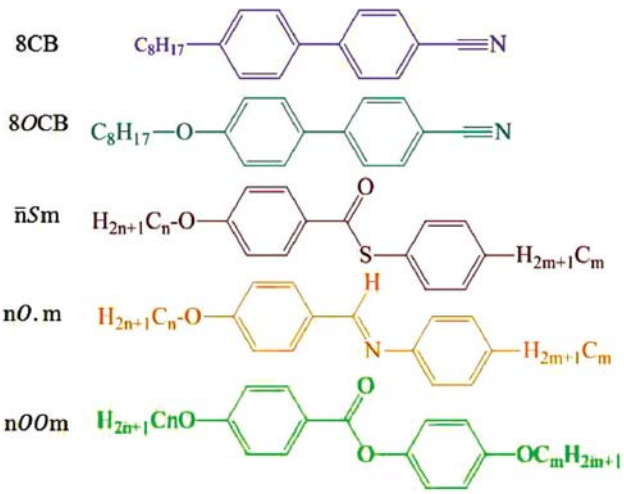

Fig. 2 — Structural formulas for liquid crystals referred in this work

be followed for another study on dispersed carbon nanotubes in 9OO4 as a function of concentration to be reported in a previous work[11].

2.1 Modulated Differential Scanning Calorimetry

Modulated (temperature) differential scanning calorimetry (MTDSC/MDSC) allows for the simultaneous measurement of the evolution of both the heat flow and heat capacity. It is essentially the combination of traditional AC-calorimetry with DSC. This method allows for measuring the total heat flow (enthalpy) as well as its non-reversible (kinetic or imaginary component) and the reversible (real component) heat capacities. A detailed description of the MDSC method can be found elsewhere[12-18].

MDSC experiments were performed using a Model Q200 from TA Instruments, USA. Prior to the experiment with our sample, temperature calibration was done with a sapphire disc, under the same conditions of measurements. The analysis method used to extract the complex specific heat is based on linear response theory[9,12]. In general, a temperature oscillation is described as $T(t) = T_0 + q_0 t + AT \sin(\omega t)$ where T_0 is the initial temperature at time $t = 0$, T is the absolute temperature at time t, q_0 is the baseline temperature scan rate, A_T is the temperature amplitude, and ω ($\omega = 2\pi f$) is the angular frequency of the temperature modulation. The temperature rate is also time dependent given by $q(t) = dT/dt = q_0 + A_q \cos(\omega t)$ where A_q is the amplitude of the temperature modulation rate ($A_q = \omega A_T$). Since the applied temperature rate consists of two components, q_0 the underlying rate and $A_q \cos(\omega t)$ the periodic rate, the measured heat flow $H\,F$ can also be separated into two components in response to these rates. The periodic component can be described as $H\,F_q = A_{HF} \cos(\omega t - \varphi)$ where A_{HF} is the amplitude of the heat flow and φ is the phase angle between heat flow and temperature rate. The absolute value of the complete specific heat is written as $C^*_p = A_{HF}/mA_q$ where m is the mass of the sample. The phase angle requires a small correction (calibration) to account for finite thermal conductivities of the sample and cell, see Ref. (18). The real (reversible) C'_p and imaginary (non-reversible) C''_p parts of the specific heat are then given by:

$$C'_{\mathrm{p}} = C^*_p \cos(\varphi) \qquad \ldots(1)$$

$$C''_{\mathrm{p}} = C^*_p \cos(\varphi) \qquad \ldots(2)$$

That allows for a consistent definition of the complex specific heat. Typically, under equilibrium conditions, $C'_p = 0$, after φ correction (or have a weak linear temperature dependence remaining). The appearance of a peak-like non-zero C'_p feature commensurate with a peak in the real part of the specific heat indicates that this feature is a first-order transition and involves a latent heat.

The MDSC experiment was carried out with a constant dry ultra-pure nitrogen gas flow rate of 40 ml/min during all runs. For accurate measurement of specific heat or to decrease the uncertainty, the reference and the sample hermitically sealed *Al* pans were chosen carefully. The mass of the reference *Al* pan used was 0.0504 g that closely matches the sample cell pan and the sample mass was 0.012 g. Various heating and cooling temperature scan rates as well as a range of temperature modulation amplitudes and periods were performed in order to estimate the closest approximation to quasi-static (near-equilibrium) results. Scans were performed between 25°C (298.15 K) and 95°C (368.15 K), first cooling followed by heating scans. Degrees Celsius will be used hereafter to report the absolute temperature. The final chosen modulation parameters were 0.5 K for the amplitude and 120 s (2 min) for the period with a baseline scan rate of ±0.3 K/min. Note that the modulation rate is slightly faster than the baseline rate, which appears necessary for the Q200 instrument to yield good results. Each scan cycle of cooling followed by heating was repeated twice in order to ensure reproducibility.

The excess specific heats were determined in order to isolate the contribution from the various transitions. A linear baseline was used over the entire temperature scan range in order to determine $\Delta C_p = C_p - C_{\text{baseline}}$ for both the real and imaginary components, though C'_p always exhibited a very shallow linear baseline that was very close to zero (flat) indicating near-equilibrium conditions for the experimental parameters chosen. For specific heat features that are close in temperature, the wing of one peak (usually the higher temperature peak) typically is subtracted from the lower specific heat peak in order to isolate the excess specific heat of a given transition, denoted as $\delta C_p = \Delta C_p - C_{\text{wing}}$ where C_{wing} is an empirical mimic function of the underlying wing. This calculation was only applied to the real component of the specific heat.

The particular transition enthalpy component is simply the integration of the excess specific heat component over a given temperature range, e.g $\Delta H'_{IN} = \int \Delta C'_p \, dT$ for the real and $\Delta H''_{IN} = \int \Delta C''_p \, dT$ for the imaginary enthalpy. The total transition enthalpy is defined as:

$$\Delta H = \sqrt{(\Delta H')^2 + (\Delta H'')^2} \, .$$

2.2 Dielectric spectroscopy

Dielectric measurements were performed on a home build dielectric spectrometer using a General Radio 1615-A AC-capacitance bridge, a Stanford Research SR830 DSP lock-in-amplifier, a Lakeshore 310 temperature control with a Mettler hot-stage, and an Instec liquid crystal cell primarily used for electro-optical (switching) experiments as the capacitive sample cell. The instrument has a temperature stability of better than ±0.01 K, a wide scan rate capability, and a frequency range of about 10 Hz to 105 kHz. The procedure requires the empty cell's capacitance C_{empty} to be measured prior to filling with sample. The dielectric constant is then determined by the ratio of $\varepsilon = C_{\text{filled}}/C_{\text{empty}}$, where the real part is the in-phase and imaginary part is the out-of-phase parts of the LIA signal.

Measurements were performed on a sample of 9OO4 taken from the same batch as the sample used for the calorimetry measurements. Two Instec electro-optical cells, one with homeotropic (perpendicular) and the other homogeneous (anti-parallel rubbed, planar) surface alignment each having a 10 × 10 mm area and 20 μm gap, were filled in the isotropic phase of 9OO4 then thermally cycled between the isotropic and nematic phases a few times to ensure complete filling and alignment. Uniform alignment was observed by polarizing optical microscopy. Temperature scan dielectric measurements used 1 V as the excitation voltage amplitude at 100 kHz with a scan rate of 0.3 K/min, first cooling then heating and were repeated twice. Switching experiments were performed in the Crystal, Sm*C* and N phases using 100 kHz voltages that ranged from 0.5 to 36 V (electric fields of 0.05 to 1.75 V/μm) for both cells. Again, the switching experiments were repeated twice. For both the temperature scan and voltage scan experiments, the results were reproducible to well within 1 %.

3 Results

3.1 Calorimetry

The overview of the excess reversible C'_p and non-reversible C''_p specific heat taken first on cooling then on heating using the quasi-static parameters, is shown in Fig. 3. It should be noted that the cooling scan was paused at 47°C for <2 h in order to allow for the Sm*B* phase to fully form before the cooling scan proceeded. On cooling, 9OO4 exhibits the phase sequence *I*-*N*-Sm*A*-Sm*C*-Sm*B*-Crystal (*K*) while on heating, melting occurs nearly 25 K higher that is followed by a specific heat peak almost 2 K higher before entering the Sm*A* phase. Further heating yields the *N* and *I* phases. Based on C''_p behaviour, the *I*-*N* is weakly first order, the N-SmA is continuous, the Sm*A*-Sm*C* is continuous, the Sm*C*-Sm*B* is first order, and the Sm*B*-*K* is strongly first-order. The strongly first-order melting followed by a second, first-order, C_p feature indicates the presence of an intermediate phase (labeled Sm*X*) between *K* and Sm*A* on heating. For all transitions temperatures, we take the temperature of the $\Delta C'_p$ peaks (T_{IN}, T_{NA}, T_{AC}, T_{CB}, T_{BK}, T_{KX}, T_{XA}). These transition temperatures on cooling and heating as well as the two-phase co-existence range (the range of non-zero $\Delta C''_p$) and the transition temperature hysteresis (difference of T_C on heating and cooling) are summarized in Table 1.

For the *I*-*N* phase transition, the real and imaginary excess specific heat signatures are typical for this weakly first-order transition (Fig. 4). The transition hysteresis is $\delta T_{\text{hyst}} = T^h_{IN} - T^c_{IN} = +0.01$ K where the non-zero non-reversible part of the specific heat does not show a simple peak, as is typical for a pure AC-calorimetric method[19]. The character of the non-zero

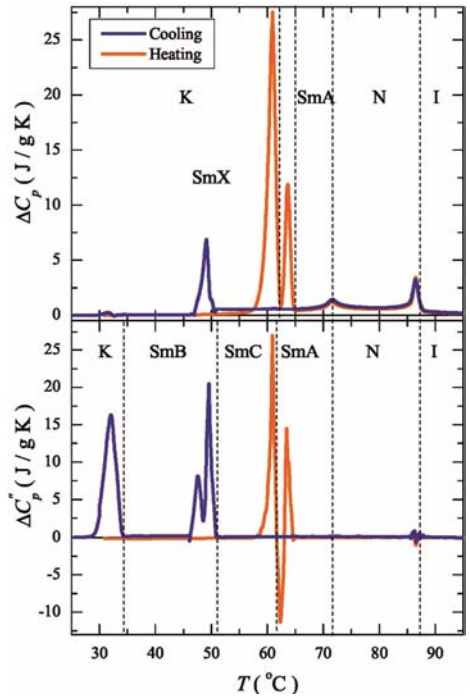

Fig. 3 — Overview of the excess reversible (top panel) and non-reversible (bottom panel) specific heat on cooling then heating between <95 and 25°C by MDSC. This excess specific heat was determined by subtracting a linear background over the entire experimental temperature range from the reversible and non-reversible specific heat. Scans were performed using parameters that most closely approximated static heat capacity results; a base scan rate of ±0.3 K/min and an induced temperature amplitude of 0.5 K at 120 s heating period. Note that the cooling scan was paused at 47°C (320.2 K) for <2 h before continuing.

Table 1 — Summary of the transition temperatures T_C for 9OO4 based on the quasi-static MDSC results for both cooling and heating scans (superscripts c and h, respectively) in celsius. First-order transition temperatures are taken as the highest temperature of the two-phase coexistence range (or the lowest temperature of the higher temperature phase) determined from the non-reversible (imaginary) part of the specific heat, $\Delta C''_p$. Continuous-order transition temperatures are taken as the temperature of the peak in the reversible $\Delta C'_p$ for the *N*-Sm*A* transition or the inflection point of the high temperature side of the $\Delta C'_p$ peak for the Sm*A*-Sm*C* transition. The two-phase coexistence range δT_{2p} and the transition temperature hysteresis δT_C are also shown. If the transition is monotropic, it is designated mono. Uncertainties stem from determining the onset of non-zero, $\Delta C''_p$.

Transition	T^c_C	T^h_C	δT_{2p}	δT_C
I-*N*	86.20 ± 0.06	86.49 ± 0.04	2.3 ± 0.2	0.27
N-Sm*A*	71.49 ± 0.09	71.68 ± 0.05	0	0.15
Sm*A*-Sm*C*	61.10 ± 0.08	–	0	mono
Sm*C*-Sm*B*	49.38 ± 0.04	–	4.6	Mono
Sm*B*-*K*	35.30 ± 0.02	–	5.8	mono
K-Sm*X*	–	60.92 ± 0.09	3.9	mono
Sm*X*-Sm*A*	–	63.64 ± 0.08	2.1	Mono

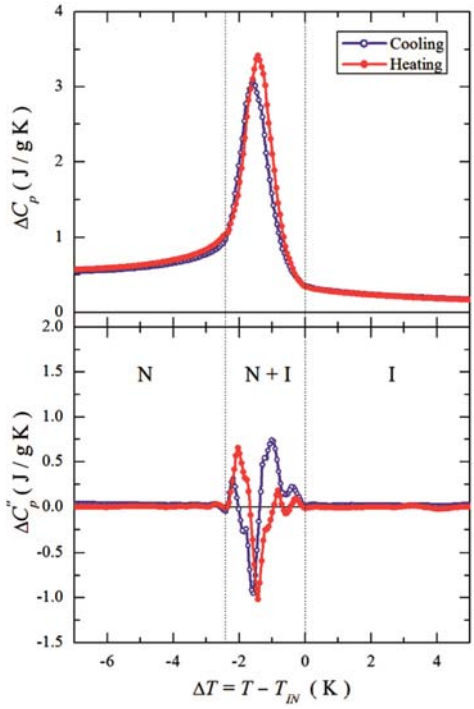

Fig. 4 — Detailed view of the excess reversible (top panel) and non-reversible (bottom panel) specific heat about the isotropic to nematic phase transition on cooling then heating about the transition temperature $T_{IN} = T - T_{IN}$. Quasi-static parameters of Fig. 3 were used for these scans. For clarity, every 15th data point has been plotted. Note the indication of the two-phase (I+N) coexistence range by the vertical dashed lines was determined by the non-zero signal in $\Delta C''$

$\Delta C''$ region is that of an oscillation rather than a peak as shown in Fig. 4, indicating that the phase shift angle has aliased within the *I* +*N* coexistence range, which can happen in the Fourier Transform analysis method of MDSC. On cooling, the effective enthalpy components for the *I*-*N* phase transition are $\delta H' = 3.91 \pm 0.08$ J/g and $\delta H'' = 0.98 \pm 0.08$ J/g yielding a total *I*-*N* transition enthalpy of $\Delta H_{IN} = 5.85 \pm 0.08$ J/g. There is an observed difference of about 0.96 ± 0.0 J/g in total enthalpy for the *I*-*N* transition. Total transition enthalpy values are summarized in Table 2. These results are consistent with the *I*-*N* phase transition being a weakly first-order phase transition typical of liquid crystals.

The *N*-Sm*A* phase transition does not exhibit any feature in the imaginary specific heat indicating the lack of a latent heat. The excess real part of the specific heat is isolated by using a simple polynomial to model the low-temperature wing of the *I*-*N* transition that underlies the *N*–Sm*A*. The resulting

real $\delta C'_p$ on cooling then heating as a function of temperature about T_{NA} is shown in Fig. 5. There is a small hysteresis in T_{NA} between heating and cooling of about $\delta T_{hyst} \sim +0.15$ K, much larger than that observed for the *I*-*N* transition. While the $\delta C'_p$ wings overlap very well, the peak is larger on heating than on cooling. This is reflected by a larger real enthalpy (equal to the total enthalpy since $\Delta H''_{NA} = 0$) on heating than cooling $\Delta H'_{NA} = 3.22$J/g versus 3.02 J/g, respectively) well outside the estimated uncertainties of ~ 0.1 J/g. Despite the hysteresis behaviour, reproducible after multiple cooling and heating cycles, the *N*-Sm*A* transition for 9OO4 is continuous.

Table 2 — Summary of the transition enthalpies for 9OO4 based on the quasi-static MDSC results for both cooling (c) and heating (h) scans. The transition enthalpy, ΔH, is determined as the root-mean-square of the reversible (real, $\delta H'$) and non-reversible (imaginary, $\delta H''$) enthalpy in Joules per g. Uncertainties represent integration error, overall uncertainties in determining enthalpy by MDSC is about 10%

Transition	ΔH^c	ΔH^h	$< H >$
I-*N*	4.89 ± 0.08	5.85 ± 0.08	5.4 ± 0.1
N-Sm*A*	3.02 ± 0.06	3.32 ± 0.08	3.2 ± 0.1
Sm*A*-Sm*C*	0.32 ± 0.08	–	0.3 ± 0.1
Sm*C*-Sm*B*	45.53 ± 0.08	–	45.5 ± 0.1
Sm*B*-*K*	38.83 ± 0.08	–	38.9 ± 0.1
K-Sm*X*	–	72.12 ± 0.09	72.1 ± 0.1
Sm*X*-Sm*A*	–	32.39 ± 0.08	32.4 ± 0.1
Total	92.8 ± 0.2	113.4 ± 0.2	103.1 ± 0.2

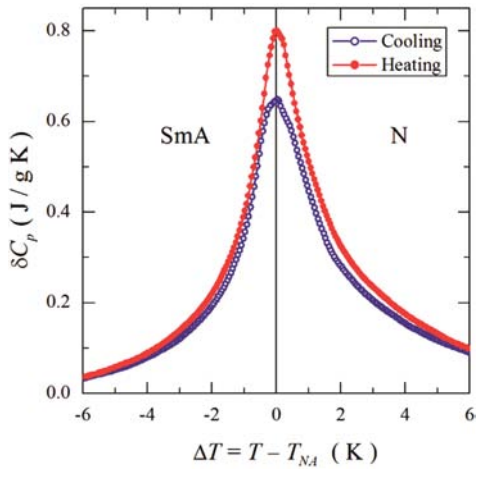

Fig. 5 — Excess reversible specific heat for the nematic to smectic-A phase transition on cooling then heating about the transition temperature T_{NA}=T–T_{NA} using the quasi-static experiment parameters of Fig. 3. For clarity, every 15th data point has been plotted. This excess specific heat was determined by subtraction of the low-temperature specific heat wing of the *I*-*N* phase transition. Note that the non-reversible specific heat was essentially zero through this transition, indicating the continuous character of this transition

The excess specific heat of the Sm*A*-Sm*C* phase transition δC_{AC} was isolated by sub-tracting the low temperature wing of the *N*–Sm*A*, C_p peak and is shown in Fig. 6. The δC_{AC} peak is monotropic and exhibits no imaginary C_p feature. Given the shape and continuous nature of the transition, it is classified as a Landau (mean-field) second-order transition[3].

The Sm*A*-Sm*C* phase transition temperature T_{AC} is taken as the temperature of the δC_{AC} peak yielding T_{AC} = 61.1°C. The effective transition enthalpy $\delta H'_{AC}$ = 0.32 ± 0.08 J/g, determined by integrating δC_{AC} from about 2 K above T_{AC} down to temperature of the Sm*C*-Sm*B* transition, is typical for this transition.

The excess specific heat ΔC_p of the Sm*B* temperature range on cooling is shown in Fig. 7 as a function of baseline scan rate from 0.3 to 0.7 K/min with the modulation parameters were kept fixed. Clear observations of scan rate dependent are seen in both the real and imaginary parts of the specific heat. The Sm*C*-Sm*B* transition is marked by a strongly first-order specific heat signature at T_{CB} = 49.38°C with the imaginary C_p peak being much larger than the real C_p peak and both peaks generally decrease in amplitude with increasing scan rate. Specifically, as the scan rate increase from 0.3 to 0.7 K/min the

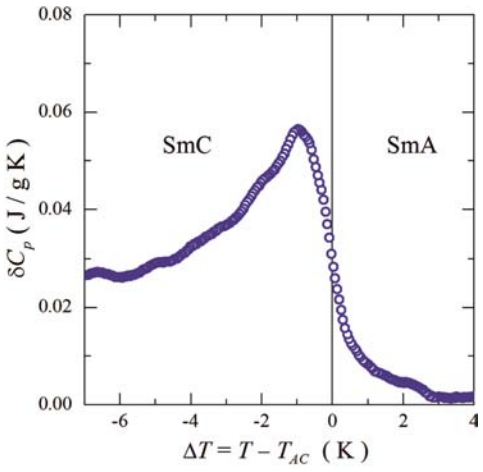

Fig. 6 — Excess reversible specific heat for the smectic-A to smectic-C phase transition on cooling about the transition temperature T_{AC} =T − T_{AC} using the quasi-static experiment parameters of Fig. 3. For clarity, every 15th data point has been plotted. The transition temperature was estimated by the inflection point of δC_p on cooling. This excess specific heat was determined by subtraction of the low-temperature specific heat wing of the *N*-Sm*A* phase transition underlying the Sm*A*-Sm*C* transition. Note that non-reversible specific heat was essentially zero through this transition, indicating the continuous character of this transition

enthalpy components of the Sm*C*-Sm*B* transition decrease; the total enthalpy decreases smoothly from ~ 46 to 35 J/g, respectively. Surprisingly, given the very low scan rates employed, as the temperature continuously cools, several $\Delta C''_p$ signatures are observed that are highly baseline scan rate dependent, in general smearing out over the entire Sm*B* temperature range as the scan rate increases. As the scan rate increases, the real component of $\Delta C'_p$ increasingly exhibits small modulations that also increase in amplitude(Fig. 7). The Sm*B* phase on cooling ends with strongly first-order C_p signatures of crystallization at T_{BK} ~ 35.3°C having a very small real component and a very large imaginary component. In general, the integrated enthalpy over this entire temperature range is only weakly scan rate dependent indicating that these multiple complex features are due to very slow conversion from the

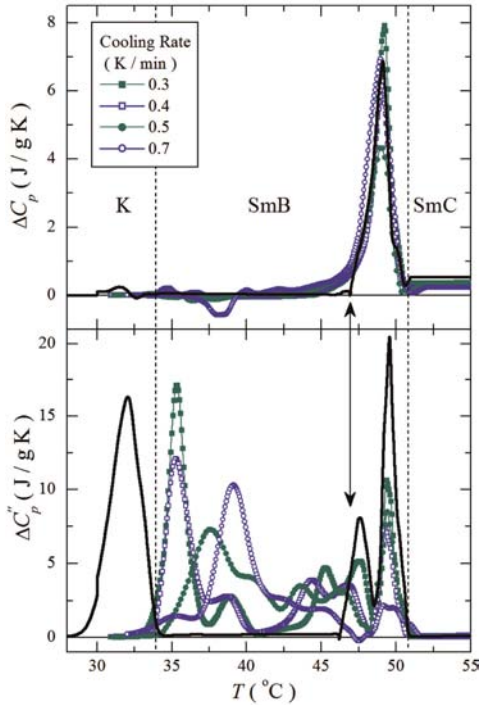

Fig. 7 — Reversible and non-reversible excess specific heat on cooling over the smectic-*C* to smectic-B to crystallization transitions as a function of continuous scan rate. For clarity, every 15th data point has been plotted. Quasi-static modulation parameters were used; 0.5 K temperature amplitude and 120 s heating period, while the cooling rate was varied from the lowest of 0.3 to 0.7 K/min (See legend). The base rate cooling scan is shown at 0.3 K/min that was paused at 47°C for 2 h before proceeding (solid line), the pause point is indicated by the vertical double arrows. The vertical dashed lines approximate the first-order Sm*C*-Sm*B* and Sm*B*-*K* transitions. (See Fig. 7 and related text for a discussion of the Sm*C* to Sm*B* behavior)

Sm*C* to the Sm*B* phase. To test this, a cooling scan using the quasi-equilibrium parameters was performed where the scan was stopped just below T_{CB} at 47°C for 2 h then resumed. This scan, shown as the solid line in Fig. 7 where the scan pause is indicated by the vertical double arrow, still found a small $\Delta C''_p$ below the large one associated with the Sm*C*-Sm*B* transition but prior to the pause. However, no other feature is observed in either the real or imaginary components until crystallization is reached at a lower temperature of T_{BK} = 32°C. This is consistent since a not fully formed Sm*B* phase would provide many nucleation sites for crystallization to occur and so be at a higher temperature when the scan was continuous.

Upon heating under continuous quasi-equilibrium conditions, the crystal phase super heats until a strongly first-order specific heat feature is observed that ends at ~ 61°C.

Upon further heating, a second first-order feature is seen nearby that ends when the Sm*A* phase appears at ~ 64°C (Fig. 8). Because of the slow Sm*B* phase conversion observed on cooling, a similar scan rate study was done over the same range of rates on heating and these are also shown in Fig. 8. Here, the melting *C*p peak, generally, decreases in amplitude and smears in temperature with an effective total enthalpy of δH_{KX} =0 72 J/g and an effective total enthalpy of the second feature of δH_{XA} =0 32 J/g. Interestingly, the second feature decreases in size rapidly with increasing scan rate, suggesting that the melting of *K* phase is not clear from MDSC data due to rapid scan rates. Because of the magnitude of the enthalpy involved, it is possible that this feature is a transition into an intermediate smectic phase before heating into the Sm*A* phase. We denote this phase as Sm*X* and are unclear as to whether this phase is Sm*B* or Sm*C* like since the melting occurs very near T_{AC} on cooling. The remaining transitions from Sm*A*-*N* and *N*-*I* exhibit specific heat features consistent with that seen on cooling and those typical in the literature. A summary of the transition temperatures are given in Table 1 and total transition enthalpy on heating, cooling, and their average are given in Table 2. The total enthalpy of all phase transitions from the crystal to isotropic phases is given, which is on average 103 J/g. This total shows a difference of about 21 J/g between heating and cooling that is within <10% of each other, which is about the uncertainty of the absolute enthalpy for this technique.

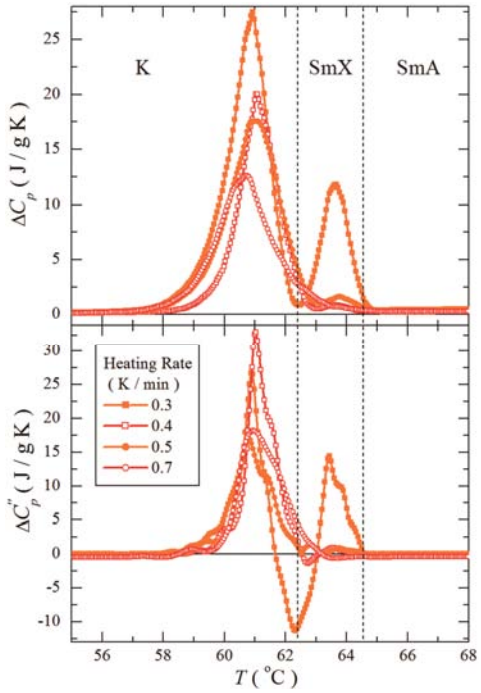

Fig. 8 — Reversible and non-reversible excess specific heat on heating from the melting to smectic-A transitions as a function of continuous scan rate. For clarity, every 15th data point has been plotted. Quasi-static modulation parameters were used; 0.5 K temperature amplitude and 120 S heating period, while the cooling rate was varied from the lowest of 0.3 to 0.7 K/min (See legend). The vertical dashed lines approximate the transitions from the crystal to an undetermined smectic phase denoted Sm*X* and another from Sm*X* to the Sm*A* phase. Both observed transitions are first-order

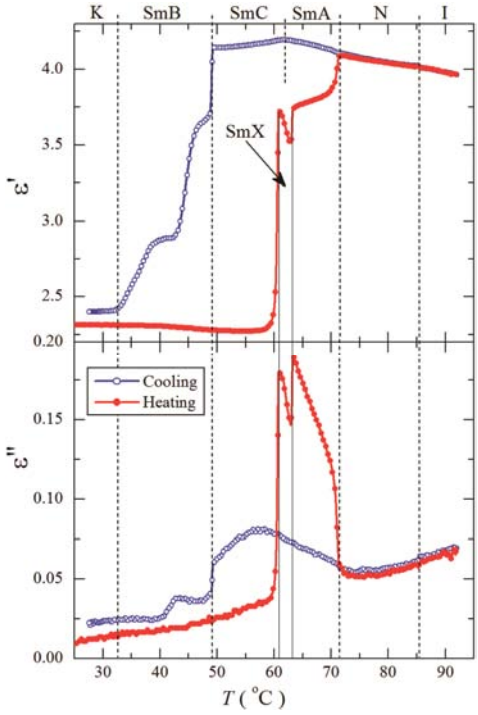

Fig. 9 — Real ε′ (top panel) and imaginary ε″ (bottom panel) dielectric constant of 9OO4 in the homogeneous (planar) cell. Data taken on cooling then heating at 100 kHz using ±0.3 K/min scan rates between 95 and 25°C (See legend). For clarity, every 10th data point has been plotted. The vertical dashed lines indicate the *I*-*N*, *N*-SmA and the Sm*C*-Sm*B* (cooling only) transitions

3.2 Dielectric spectroscopy

In order to illuminate the transition features as well as explore the slow phase conversions observed, dielectric measurements were performed at a frequency of 100 kHz on the two capacitive cells each having the same active area and gap but differ in alignment for both temperature and voltage switching scans. All dielectric measurements were carried out over the same temperature range using the same baseline scan rate of ±0.3 K/min as was used in the MDSC measurements. Thus, the dielectric and calorimetry measurements experienced the same thermal conditions. The multiple scanning cycles were done and found very good reproducibility.

Cooling then heating scans for the real ε′ and imaginary ε″ components of the dielectric constant for the homogeneous (planar) aligned cells are shown in Fig. 9. This cell alignment has the long axis of the LC molecule parallel to the surface and its dipole moment parallel to the applied electric field. On cooling, a very small feature is observed in ε′ and ε″ through the *I*-*N* and *N*-Sm*A* transition with ε′ increasing with decreasing temperature, both 0.2 K of the specific features for these transitions. However, ε″ decreases with decreasing temperature until the *N*-Sm*A* transition where it sharply changes slope and begins to increase with decreasing temperature. Upon further continuous cooling, the real component ε′ sharply changes slope and begins to smoothly decrease with decreasing temperature with no discernable feature seen in ε″ at the Sm*A*-Sm*C* transition. Approximately mid-range of the Sm*C* phase while ε′ continuous to decrease smoothly, ε″ exhibits a broad peak at ~ 56°C then decreases continuously with decreasing temperature until the Sm*C*-Sm*B* transition. At the Sm*C*-Sm*B* transition, both ε′ and ε″ exhibit a sharp decrease within 0.1 K of T_{CB} observed by calorimetry. Cooling through the Sm*B* phase continuously, a single step-like feature is seen in ε′ commensurate with a small peak in ε″. The onset of crystallization is marked by a sudden temperature independent of ε′ and

no signature in ε''. This onset matches well with the temperature for crystallization seen in the calorimetry under continuous cooling (See Figs 3 and 9).

On heating, ε'' smoothly increases with increasing temperature while ε' is essentially constant until about 40°C where it begins to very slightly decrease. When melting is reached, there is a very sharp increase in both components of ε followed immediately by a decrease in value until another sharp increase in both is observed < 2 K higher. As seen in Fig. 9, the jump in ε' does not reach the value on cooling while ε'' is much larger than that seen on cooling in the Sm*A* phase. The heating only matches the cooling values above the *N* –Sm*A* transition; in the nematic and isotropic phases. Again, all dielectric features observed correlate very closely to those observed by calorimetry.

Voltage scans between 0.5 and 36 V across the 20 µm gap found no switching change in either ε' or ε'' for the homogeneous (planar) aligned cell in either the crystal, Sm*C*, or *N* phases. This is consistent with the negative dielectric anisotropy of 9OO4 and indicating that the results described and shown in Fig. 9 should be independent of applied electric field. However, voltage scans for the homeotropic (perpendicular) aligned cell found a strong switching behaviour where ε' begins to increase at ~ 4 V, shown an inflection at ~ 9 V, nearly satuarating at 36 V in the nematic phase (77°C) yielding a $\Delta\,\varepsilon' = 0.16$. Over this voltage range ε'' decreases slightly from 0.315 to 0.305. No switching behaviour is observed for the homeotropic cell in the Sm*C* or crystal phases of 9OO4, as expected for these higher-order phases.

The temperature scans for the homeotropic cell were conducted at 0.5 V and 35 V on cooling then heating using ±0.3 K/min for consistency. The cooling at 0.5 V reproduces the magnitude and temperature dependence of the homogeneous cell shown in Fig. 9 in the isotropic phase. However, upon entering the nematic phase, ε' begins to decrease strongly from about 4 near *I*-*N* to ~ 3 just above the Sm*B*-Sm*C* transition with small features indicating the *N*-Sm*A* and the Sm*A*-Sm*C* transitions. Once in the Sm*B* phase at ~48°C, the low voltage scan shows a sharp step down for ε' to 2.6 then constant for 3 K when it steps up broadly over nearly 2 K back to ~2.9 at ~ 43°C. On further cooling, ε' remains nearly constant until ~ 35°C where it begins to smoothly decrease to 2.5 at ~ 30°C completing the entry into the crystal phase. Cooling scans in the switched state using 35 V nearly reproduce exactly ε' for the homogeneous cell, indicating a uniform and complete switch of the cell, except for the temperature range just in the Sm*B* phase. For the switched cell, beginning at ~ 48°C, ε' remains at ~ 3.1 with only a very small feature marking the 5 K range where the unswitched cell saw a step-down-step-up behaviour. The onset process for crystallization begins at ~ 37°C and is completed at the same temperature of 30°C. In contrast, the homogeneous cell data reveals an initial step once the Sm*B* phase is entered the intermediate between the Sm*C* value and the plateau value prior to crystallization. On heating, the low and high voltage scans (unswitched and switched) reproduce each other and the homogeneous cell ε' up to the *N*-Sm*A* transition. The switched homeotropic cell follows closely the homogeneous cell while the unswitched homeotropic cell reproduces its cooling scan. It should be noted that the dispersion ε'' for the homeotropic cell has the same temperature dependence in shape but larger in magnitude by a factor of 10, indicating that the frustration for the molecular surface alignment and the direction of the dipole moment for 9OO4 in a homeotropic cell leads to much larger dispersion losses. All these voltage and temperature scan results indicate that 9OO4 has a strongly temperature dependent negative dielectric anisotropy below the *I*-*N* transition similar to that of 4O.8 and 8S5. Also, there is a 5 K temperature range just below the Sm*B*-Sm*C* transition where the ordering is difficult to establish, presumably because of the frustration between the steric interactions of the molecule and the perpendicular dipole moment.

4 Discussion and Conclusions

Figure 2 shows the phase ordering of 9OO4 presented in this work have four notable features as compared to the two similar LCs 8S5 and 4O.8. Firstly, 9OO4 and 8S5 exhibit two monotropic smectic phases, the Sm*C* and Sm*B* phases. Secondly, the *N*-Sm*A* transition in 9OO4 has an unusually small enthalpy of 0.3 J/g as compared to that in 8S5 and 4O.8 of about 2 J/g. Thirdly, the conversion into the Sm*B* phase is very slow, exhibiting strong variations and multiple steps even for very slow scan rates. Finally, on heating 9OO4 exhibits a stable specific heat and dielectric feature that indicates an intermediate smectic-like phase between the crystal and smectic-*A* phase.

These results can be understood in terms of a combination of molecular packing and the influence of the unusual effective dipole moment of 9OO4. An analysis of the (volume) thermal expansion coefficient αV and the X-ray scattering measured smectic layer-spacing for the n⁻S5 series was analyzed in terms of two linear thermal expansion coefficient components parallel $\alpha_{\parallel}$ and perpendicular $\alpha_{\perp}$ to the smectic-*A* layer normal and found that $\alpha_{\parallel} < 0$ and diverges towards negative infinity upon approaching[20] *N*-Sm*A* from below. From a similar Pippard analysis, 4O.8 was found to have $\alpha_{\parallel} = 0$ as well as many members of the nO.m series. The difference between 8S5 and 4O.8 behaviour was determined to be due to the flexible-C(O)-S-linking group for 8S5 as compared to the rigid -C(H)=N- linking group for 4O.8 between their aromatic rings[20]. Both of these LCs have a slightly bent core with their two phenyl rings twisted with respect to each other. This structure is also expected for 9OO4 and supported by molecular modeling[11]. From Fig. 10 of Ref. (20), the n⁻S5 and 4O.m series follow the same trend on a log(δH_{NA}) versus McMillan ratio $R_M \equiv T_{NA}/T_{IN}$ while the nCB and nOCB liquid crystal series follow a parallel trend but nearly an order of magnitude smaller enthalpy. The *N*-Sm*A* enthalpy for 9OO4 have $R_M = 0.959$ is nearly along the trend for the polar nCB and nOCB series rather than that for the series of similar structure. Unfortunately, the quality of the MDSC data does not allow for detailed power-law analysis to extract the *N*-Sm*A* or the Sm*C*-Sm*A* critical behaviour, but the enthalpy of the *N*-Sm*A* suggests a behaviour similar to the nCB/nOCB series and the shape of the Sm*C*-Sm*A* closely resembles that expected[3]. Overall, the comparisons and observations suggest that the –C(=O)–O-linking group for 9OO4 is as flexible as that for the 8S5 linking group but with a differently oriented in-plane dipole moment that would lead to Sm*B*-like ordering. The possibility of the in-plane dipole moments pairing, forming perhaps a cybotactic group, would indicate that the smectic-*A* phase for 9OO4 is a partial bi-layer (SmA_d) rather than the monomeric smectic-*A* (Sm*Am*) of either 8S5 or 4O.8. This may also lead to the unusually slow Sm*B* phase conversion and appearance of an intermediate smectic phase on heating.

The observations presented in this work for the liquid crystal 9OO4 have revealed an interplay between the LC ordering due to molecular shape (steric) and a perpendicularly aligned dipole moment. These interactions emerge directly from the particular molecular structure of 9OO4 and can be placed now in context with other LCs of similar structure. In the present work, the specific heat, dielectric constant, and molecular modeling suggest that the combination of bent/twisted core structure, the core flexibility, and orientation of the effective dipole moment lead to the onset of a monotropic Sm*B* phase that converts very slowly from a Sm*C* phase, an *N*-Sm*A* transition similar to a very different LC structure and the appearance of an intermediate smectic-like phase between melting and the Sm*A*. Detailed dielectric measurements exploring the anisotropy as a function of frequency through the various transitions would be very helpful as well as X-ray scattering to determine the smectic-*A* layer spacing behaviour. Higher resolution calorimetry would confirm the expected critical behaviour of the continuous transition.

Acknowledgement

This work was supported by the Department of Physics at WPI and a grants from the NSF award DMR-0821292 MRI.

References

1 Goodby J W, Waugh, Stein S M & Chin E, *Nature*, 337 (1989) 449.
2 Chandrashekhar S, *Liquid Crystals*, Cambridge University Press, England, (1992).
3 Gennes P G de & Prost J, The Physics of Liquid Crystals, Oxford University Press, Clarendon, Oxford, England, (1993).
4 Demus D, Goodby J W, Gray G, Spiess H & Vill V, *Handbook of Liquid Crystals*, Wiley-VCH, Canada, (1998).
5 Birge N O & Nagel S R, *Phys Rev Lett*, 54 (1985) 2674.
6 Christensen T, *J Phys Colloques*, 46 (1985) 635.
7 Birge N O, *Phys Rev B*, 34 (1986) 1631.
8 Dixon P K, *Phys Rev B*, 42 (1990) 8179.
9 Schawe J E K, *Thermochim Acta*, 271 (1996) 127.
10 Birge N O, Dixon P K & Menon N, *Thermochim Acta*, 51 (1997) 304.
11 Kalakonda P, Basu R, Nemitz I R, Rosenblatt C & Iannacchione G S, *J of Chemical Phys,* 140 (2014) 104908.
12 Schawe J E K, *Thermochim Acta*, 261 (1995) 183.
13 Coleman N J & Craig D Q M, *Int J Pharmeceut.* 135 (1996) 13.
14 Hutchinson J M & Montserrat S, *J Them Anal*, 47 (1996) 103.
15 Hensel A, Dobbertin J, Boller A & Schawe J E K, *J Therm Anal*, 46 (1996) 935.
16 Wunderlich B, *J Therm Anal*, 48 (1997) 207.
17 Aubuchon S R & Gill P S, *J Therm Anal*, 49 (1997) 1039.
18 Weyer S, Hensel A & Schick C, *Thermochim Acta*, 267 (1997) 304.
19 Finotello D, Qian S & Iannacchione G S, *Thermochim Acta*, 303 (1997) 304.
20 Anesta E, Iannacchione G S & Garland C W, *Phys Rev E*, 70 (2004) 041703.